Additive Manufacturing 58 (2022) 103072

Contents lists available at ScienceDirect

Additive Manufacturing

journal homepage: www.elsevier.com/locate/addma

# The optimisation of hot isostatic pressing treatments for enhanced mechanical and corrosion performance of stainless steel 316L produced by laser powder bed fusion

I.S. Grech [a,*], J.H. Sullivan [a], R.J. Lancaster [a], J. Plummer [b], N.P. Lavery [a]

[a] Faculty of Science & Engineering, Bay Campus, Swansea University, Swansea SA1 8EN, UK
[b] Physical Sciences Division, Defence Science and Technology Laboratory (DSTL), Ministry of Defence, Porton Down, Salisbury, UK

ARTICLE INFO

*Keywords:*
Laser powder bed fusion
Stainless steel 316L
Hot isostatic pressing
Mechanical properties
Corrosion

ABSTRACT

This work compares the mechanical and corrosion properties of 316L steel manufactured by Laser Powder Bed Fusion (LPBF) and post treated by Hot Isostatic Pressing (HIP) to wrought 316L. HIP is often used by default on LPBF components to reduce porosity and obtain the best mechanical properties, however, if the HIP temperatures are too high, there is a risk of reducing mechanical strength and corrosion resistance. The purpose of this work was to investigate the HIP parameters and understand the trade-off in properties. By choosing various HIP temperatures (700 °C, 1125 °C, 1200 °C), pressures (100 MPa, 137 MPa and 200 MPa) and hold times, optimal cycles were investigated based on the most favourable mechanical properties (density, hardness, tensile and low-cycle fatigue), and pitting corrosion resistance.

Microstructural features associated with LPBF such as melt pools, melt pool boundaries and sub granular cells were observed. These features were found to disappear with longer and higher temperature treatments, accompanied by increased grain sizes. Low and mid temperature point HIP treatments resulted in higher ultimate tensile strength but lower fracture elongation. The decreasing hardness and tensile strength trends were consistent with decreased grain boundary strengthening and decreased dislocation strengthening (with disappearing sub grain boundary and granular cells). Only one HIP condition, consisting of a low temperature and medium pressure, produced samples that achieved runout under low cycle fatigue testing for both the lower and higher stresses. Despite this, most higher temperature HIP cycles reduced the fatigue resistance. This was again attributed to the coarsening of the microstructure at the higher temperature treatments.

The spread of the pitting potentials of HIP treated samples was reduced by 52.46 % compared to the as-built material, although none were better overall compared to the wrought material. Of all the properties, porosity appears to play the most influential role on pitting corrosion, and to this extent, despite having a larger variation in results, some of the treated parts demonstrated improved pitting resistance and some demonstrated improved repassivation potentials compared to wrought 316L.

## 1. Introduction

Alloy 316L is an austenitic stainless steel that is used in numerous applications where good mechanical performance in corrosive environments is a fundamental requirement. The low carbon content of the material results in the steel being resistant to intergranular corrosion in the as-welded condition [1]. Additive manufacturing (AM) has become an increasingly popular manufacturing method as the technology has evolved significantly in recent years. Laser powder bed fusion (LPBF) is widely used, and its research and development has been of high interest to a range of industries including agriculture, defence and energy [2,3].

Despite the increased use and developments within the LPBF process, internal build defects including porosity and delaminations can typically be present in final printed parts [4]. Porosity can be sub-divided into various types, including lack-of-fusion (LoF), partially fused powder particles, gas pores and keyhole porosity [5]. For AM parts to be successfully integrated into supply chains the mechanical and corrosion performance of the materials must be predictable, repeatable and comparable to that of their wrought counterparts. Post-processing treatments such as heat treating, hot isostatic pressing (HIP) and

* Corresponding author.
*E-mail address:* 820359@swansea.ac.uk (I.S. Grech).

https://doi.org/10.1016/j.addma.2022.103072
Received 11 March 2022; Received in revised form 21 July 2022; Accepted 1 August 2022
Available online 2 August 2022

surface treating are commonly used throughout the majority of manufacturing processes to remove defects, alleviate anisotropy and improve mechanical and corrosion performance [6].

The inert gas used when building austenitic stainless steel 316L parts has also been investigated in the literature. There is a large body of published literature wherein 316L was built both in argon [7–10] and nitrogen atmospheres [11–13]. The reported effects of using argon include producing manufactured specimens with a more heterogeneous structure compared to building with nitrogen [14]. One drawback associated with using argon as a process gas is that the LPBF process can produce argon filled porosity features within parts. Due to argon not being soluble within steel these pores are unable to diffuse through the sample during HIP treatments and cannot be completely removed. Instead, these argon filled porosity features are compressed. Further heat treatment after this HIP process can result in the gas within the argon pores expanding and increasing the volume of porosity [15]. Using nitrogen in place of argon has been documented to lead to an increase in the weight percent of nitrogen within the as-built material resulting in increased material hardness [14]. Pauzon et al. state that differences in oxygen and nitrogen dissolution appeared to have little effect on the mechanical properties of the material [11]. In addition to this, Pauzon et al. presented parts built to near complete densification under both nitrogen and argon atmospheres with relative densities of $99.96 \pm 0.02$ % [11]. It is also possible to implement helium as a process gas for LPBF 316L, with thin structures built under helium exhibiting a finer cellular structure, increased yield strength and elongation at break compared to the traditional argon and nitrogen atmospheres [16]. The work outlined in this article uses the conventional argon atmosphere for the build process which is still widely used in academic and industrial settings.

HIP treatments commonly use an inert gas at elevated pressures to exert an isostatic force on a material at elevated temperatures. This process can reduce the volume of porosity and heat treat the part in a single process whilst improving mechanical properties. The increased pressure associated with HIP treatments results in the solubility of gases trapped within pores to increase; these gases then drift to the surface of the part wherein the internal pore then collapses and closes [17]. Whilst this mechanism can remove gas filled porosity it is uncertain whether the conditions necessary to consolidate unmelted powder particles trapped within the material can be met. This phenomenon has been reported in other materials but not in 316L [18]. Additionally HIP treatments are unable to remove porosity that are connected to the external surface of a part due to the ingress of the HIP treatment gas into that porosity during the treatment [18]. The importance of this is that parts can be HIP treated wherein porosity is diffused outward from the centre of the material. Following this, the outer region of the sample can be machined away to remove any remaining surface breaking porosity. Unwanted precipitation processes can occur within materials due to the extended amount of time the materials are exposed to elevated temperatures during slow HIP cooling [19]. Preventing the formation of these unwanted precipitation processes occurring during HIP treatments can be achieved by using fast cooling HIP cycles. However, the technology required for fast cooling inside the HIP unit is not yet widely used in industry [20].

Several studies have been carried out investigating the effects of HIP treatments on reducing the presence of porosity, and how it can manipulate changes to the microstructure and resulting mechanical properties of AM 316L [21]. Cegan et al. found that using higher scanning speeds in the build process resulted in irregular LoF porosity being produced in their parts. Their HIP process ran under argon gas and significantly reduced the presence of internal closed porosity but had a minor effect on open porosity [22]. Additionally, tensile data reported by Cegan et al. suggests that their HIP process reduced the yield strength of their printed parts across all of their HIP processes whilst also reducing the deviations between individual samples as printed and increasing the materials ductility [22]. A publication by Röttger et al. demonstrates that whilst the densification of cracks was achieved through HIP treating under argon, the argon gas pores within the material are compressed but cannot be sufficiently removed with subsequent heat treatment due to insolubility of argon within the steel matrix [15]. The importance of the optimisation of the HIP process is detailed by Liverani et al. who investigated the effects of HIP treatments under nitrogen on austenitic stainless steels. They reported that increasing HIP pressure from 105 to 200 MPa has no influence on final sample density suggesting that there is a cut-off point wherein increasing the pressure of the cycles further has no benefit if porosity is the primary concern [23]. The temperature of the HIP cycles carried out in the work was also sufficient to allow for complete recrystallisation of the grains, removing the microstructural features associated with the as-built AM microstructure. This simultaneously resulted in increased ductility at the expense of yield strength and hardness [23]. The work presented by Puichard et al. agrees with the tensile data reported previously wherein their HIP under argon process resulted in a decrease to the yield strength of their material. This was attributed to a recrystallisation of 50 % of their grains and the removal of dendritic cells [21].

Sanders et al. investigated the effect of porosity on the pitting potential of LPBF 316L. They determined that the highest frequency of metastable pitting and the lowest re-passivation potentials coincided with samples containing the largest distribution of pores with diameters $> 10$ μm [24]. There is no simple quantification of the performance of LPBF 316L with large variations in testing conditions and conclusions across literature. Currently, there is limited literature investigating the effects of post production HIP treatments on the pitting corrosion performance of AM 316L in sodium chloride environments. Laleh et al. investigated the variation in corrosion performance in a sodium chloride environment as a result of high temperature thermal post processing via solution annealing and water quenching [25]. This study presented a decrease in pitting corrosion resistance in parts treated at temperatures of 1100 °C and 1200 °C compared to the as-built SLM-produced specimen and those heat-treated at 900 °C and 1000 °C [25]. However, the large error bars presented in the treated parts also suggests a large degree of variability in the pitting performance of the parts compared to their as-built control [25].

The purpose of the current work is to further the existing knowledge by optimising the mechanical and corrosion properties of AM 316L produced via LPBF in an argon atmosphere using a wide range of HIP treatments. The treatments include a variety of alternative HIP cycles using different combinations of temperatures and pressure settings, whilst also considering the influence of further aging treatments. The experimental work carried out includes microscopy, hardness, tensile and fatigue tests and cyclic potentiodynamic polarisation.

## 2. Experimental methods

### 2.1. Materials and density measurements

The composition of the nitrogen gas atomised 316L powder used in this research is given in Table 1. The particle size distribution (PSD) of the powder was 0.36 % - 53 μm $>$ 45 μm, 99.55 % - 45 μm $>$ 15 μm and 0.09 % - 0 μm $<$ 15 μm as obtained from the supplier, Sandvik Osprey. Initially, a number of 316L builds were carried out to select a set of machine parameters with sufficient repeatability across the plate (inter-build) and between builds (intra-build) that would be used for the HIP study. In the interest of space, the summarised outcome of this step was that the parameters (Exposure Time = 80 μs, Point Distance = 60 μm, Hatch Spacing = 110 μm, Power = 195 W) with a combined volumetric energy density (VED of 47.27 J $mm^{-3}$) had a repeatable average density ($7.96 \pm 0.08$ g $cm^{-3}$) with a population variance of 0.0007 $g^2$ $cm^{-6}$ across the plate and of 0.0012 $g^2$ $cm^{-6}$ between builds. At these parameters the presence of porosity was believed to be limited yet consistent, allowing for the ability of the post-production treatments to remove porosity to be quantified. Density measurements were recorded

**Table 1**
Composition of stainless steel 316L powder and wrought material measured using ICP-OES and LECO, Eltra Combustion in compliance with ISO/IEC 17025:2017.

| Element | Name | Fe | Cr | Ni | Mo | Mn | Si | P | C | S |
|---|---|---|---|---|---|---|---|---|---|---|
| Composition (wt %) | Powder | Bal. | 16.9 | 12.5 | 2.4 | 0.67 | 0.6 | 0.02 | 0.019 | 0.008 |
| Composition (wt %) | Wrought material | Bal. | 17.5 | 12.0 | 2.0 | 0.94 | 0.5 | 0.04 | 0.025 | 0.001 |

on the printed cubes prior to machining using a Sigma 700 force tensiometer, utilising the Archimedes principal following ASTM B962 - 08 [26]. Once cubes were sectioned into slices, optical analysis using a Zeiss Axio Observer combined with Image J was carried out.

The parts were printed in an argon atmosphere using a Renishaw AM 400 LPBF system with each part being supported by 2 mm build scaffold structures. A total of 12 sets of parts were produced with 11 of the sets subjected to post-production treatments. The final set remained in the as-built condition. Each set contained 2 cubic samples (15 mm × 15 mm × 15 mm) 3 tensile bars and 3 cylinders which were machined into fatigue samples after treatment.

For the purposes of microscopy, hardness and corrosion testing the cubes were sectioned into 15 mm × 15 mm × 1 mm thick slices in a direction parallel to the build plate. Each sample slice was mounted using Buehler's non conducting EpoMet fine mounting compound and metallurgically prepared by surface grinding using a Buehler Hercules SiC disc followed by polishing to a 1 μm finish using Buehler MetaDi supreme polycrystalline suspension for each token.

A 1.2 mm thick wrought annealed sheet of proprietary recipe 316L was sourced from Goodfellow Cambridge Ltd and was sectioned into 10 mm × 10 mm sized samples for hardness, microscopy and corrosion testing. NaCl, and all other chemicals used, were obtained from Sigma Aldrich and were of analytic grade purity. Unless stated otherwise all of the work detailed in this paper was carried out at standard room temperature and pressure.

### 2.2. HIP parameter matrix of experiments

For the HIP parameter experimentation, a midpoint temperature of 1125 °C and pressure of 137 MPa were selected based on nominal values in the literature [6], and known to be used in industry by default. The ramp and cooling rates were kept at 2.5 K/minute for all HIP runs, and default soak duration was 4 h, except for one experiment which was held for 60 h. In the experiments, cycles are assigned a low, medium and high parameter for both temperature and pressure as well as a long hold cycle held for 60 h. The temperature points chosen for the HIP cycles were 50 % (700 °C), 80 % (1125 °C) and 85 % (1200 °C) of the melting point of 316L with the aim of medium and high points being either side of the phase transition line between the gamma and gamma + delta regions in the material's phase diagram. In terms of notation, the different material conditions have been labelled as # - HIP ($T_x$ $P_y$), wherein # represents the condition number, and x and y represent the HIP treatment temperature (°C) and pressure (MPa).

Parts were mounted in the HIP vessel using a custom made 99.5 % alumina oxide ($Al_2O_3$) stand to hold each part vertically upright during HIP treating. The stand allowed for 1 cube, 3 tensile specimens and 2 cylinders to be treated in one HIP cycle. Table 2 displays the sample nomenclature associated with each condition.

### 2.3. Microscopy

Microstructural images were captured at various magnifications using a Zeiss Axio Observer and a Keyence vhx-7000 light microscopes. For each material, images were recorded perpendicular to the build direction in the X-Y orientation. Electron imaging was carried out using a JEOL JSM-6010PLUS/LA. Grain sizes were measured using a combination of the ImageJ software pack and Keyence built in grain size analysis software. ImageJ grain size quantification was carried out manually. The Keyence built in software allows the user to manually threshold an image. The microscope then uses the intersection method imploring the use of vertical, horizontal, diagonal and circular lines to produce grain size measurements. For the grain size measurements, a minimum of 150 measurements were recorded per sample across multiple directions. For cell size measurements, a minimum of 8,000 cells were measured per sample. For each sample, the data was analysed and anomalous measurements were removed. Samples were etched electrolytically using 70 % nitric acid, at a voltage of 10 V for 1 min.

**Table 2**
Post processing treatments for the different 316L variants, including HIP temperature (T) and pressures (P). For each treatment, a 2.5 K/min temperature ramp and cooling rate was used during the HIP treatment.

| Condition | HIP Temperature (°C) | HIP Pressure (MPa) |
|---|---|---|
| 1 - HIP ($T_{700}$ $P_{100}$) | 700 | 100 |
| 2 - HIP ($T_{1125}$ $P_{100}$) | 1125 | 100 |
| 3 - HIP ($T_{1200}$ $P_{100}$) | 1200 | 100 |
| 4 - HIP ($T_{700}$ $P_{137}$) | 700 | 137 |
| 5 - HIP ($T_{1125}$ $P_{137}$) | 1125 | 137 |
| 6 - HIP ($T_{1200}$ $P_{137}$) | 1200 | 137 |
| 7 - HIP ($T_{700}$ $P_{200}$) | 700 | 200 |
| 8 - HIP ($T_{1125}$ $P_{200}$) | 1125 | 200 |
| 9 - HIP ($T_{1200}$ $P_{200}$) | 1200 | 200 |
| 10 - As-built | Not Applicable | Not Applicable |
| 11 - HIP ($T_{1125}$ $P_{200}$ - long hold) | 1125 | 137 |

### 2.4. Vickers hardness testing

Vickers hardness tests were carried out using a Wilson VH3300 hardness tester equipped with a diamond tip. The machine was verified using calibration samples of known hardness before use to ensure it was operating within the tolerances of the manufacturer. Testing took place on flat samples polished to a 1 μm finish. Multiple lines of 25 indents were carried out with a spacing of 0.4 mm and a force of 9.81 N on each sample in various directions.

### 2.5. Tensile testing

Tensile testing was carried out using a Tinius Olsen H25KS test frame with a 25 kN load cell. Tensile specimens were printed perpendicularly to the build plate to the subsize specimen standard outlined in ASTM E8/E8M -13a as shown in Fig. 1a and no further machining was carried out on the specimens [27]. The measured Ra surface roughness values are given in Table 3. Tensile testing was carried out to the same standard with the initial speed in the elastic region being 0.47 mm/minute and the speed to break being 12.61 mm/minute, which gives a strain rate of 0.0003 and 0.0080 $s^{-1}$ respectively. Three tests were carried out on each condition tested in a controlled laboratory environment.

### 2.6. Fatigue testing

The as printed cylinders were built such that the base of the cylinder lies flat on the build plate and the subsequent layering of powders were introduced in a vertical orientation. The cylinders were machined into fatigue specimens using a Doosan DNM 5-axis CNC machine to the dimensions and specifications shown in Fig. 1b. All specimens were finished by longitudinal polishing to a 1 μm finish, in compliance with ASTM E466-21 [28]. The measured Ra surface roughness values for the fatigue specimens are given in Table 4. Force controlled low cycle

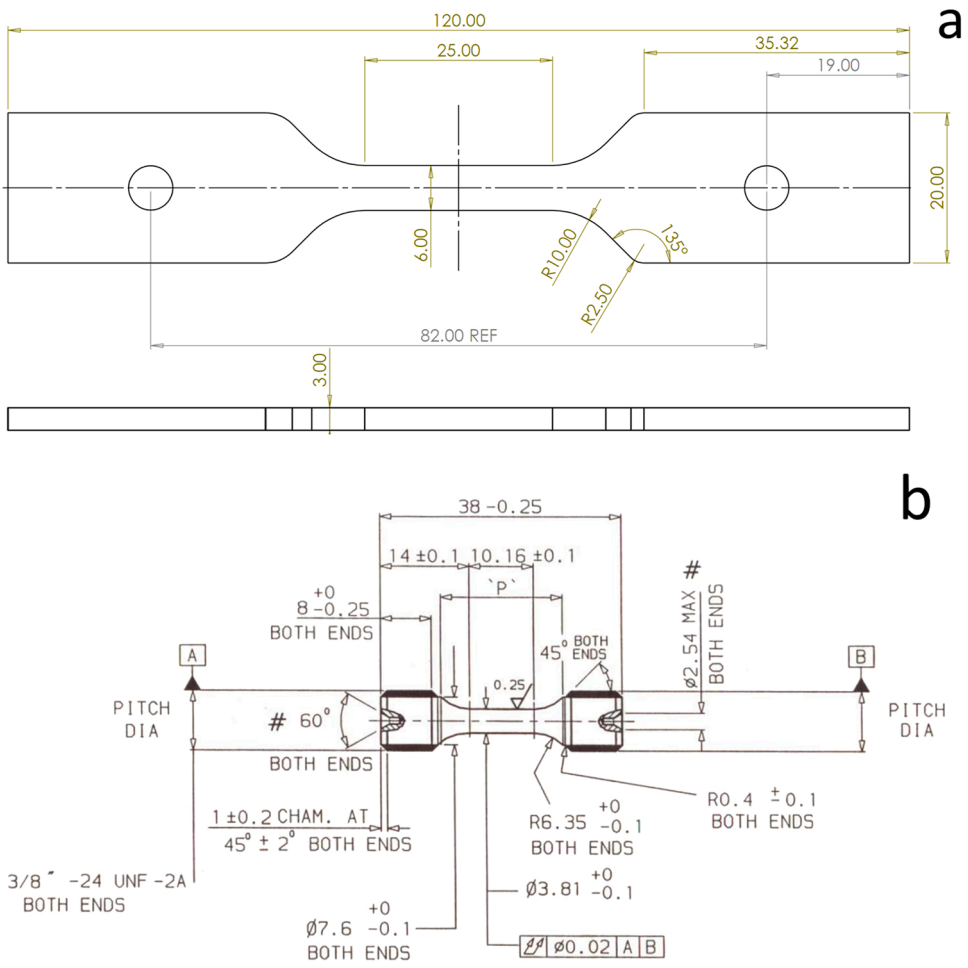


**Fig. 1.** Dimensional diagrams of a. tensile and b. fatigue specimens. Measurements given in mm.

**Table 3**
Measured Ra surface roughness values for all the tensile specimens.

| Condition | 1 | 2 | 3 | 4 | 5 | 6 | 7 | 8 | 9 | 10 | 11 |
|---|---|---|---|---|---|---|---|---|---|---|---|
| Ra (μm) | 8.7 | 8.6 | 8.5 | 8.1 | 8.4 | 8.8 | 8.4 | 7.8 | 9.0 | 10.3 | 8.9 |

**Table 4**
Measured Ra surface roughness measurements for all the fatigue specimens.

| Condition | 1 | 2 | 3 | 4 | 5 | 6 | 7 | 8 | 9 | 10 | 11 |
|---|---|---|---|---|---|---|---|---|---|---|---|
| Ra (μm) | 0.95 | 1.02 | 0.97 | 1.04 | 0.98 | 0.99 | 1.01 | 0.97 | 1.03 | 0.99 | 1.02 |

fatigue testing was carried out under two applied maximum stress levels, namely 330 and 375 MPa respectively, with a run-out limit of 100,000 cycles. An R of −1 triangular waveform with a frequency of 0.25 Hz was employed for all tests which were performed in accordance with BS EN 6072:2010 and ASTM E466–21 [28,29]. All tests were performed at ambient room temperature in a controlled laboratory environment.

### 2.7. Potentiodynamic scanning

A GAMRY 600+ potentiostat was used in a three-electrode setup with the sample acting as the working electrode for cyclic potentiodynamic polarisation [30]. The reference electrode employed was a saturated calomel electrode and a platinum-plated electrode was used as the counter. The reference electrode was placed as close to the working electrode as possible, whilst the counter electrode was placed as far away from the working electrode as possible within the confines of the system. The system was sealed using parafilm to prevent ambient atmosphere ingress. 3.5 % NaCl solution was used as the conducting solution which was deaerated by purging using nitrogen gas for 15 min prior to each experiment starting. Once purging was complete nitrogen was slowly pumped into the atmosphere of the test throughout the experiment without perturbing the solution surface. Potentiodynamic scans were initiated 200 mV below the open circuit potential scanning in the positive direction at a rate of 0.166 mV/s. The scan direction was reversed once a current density of 10 mA was recorded with the test concluding once the original starting potential was reached. These parameters were selected to allow for pitting to occur within the material and to allow for repassivation to take place. Experiments were conducted according to ASTM standards G 61–86 [31] and G 59–97 [32].

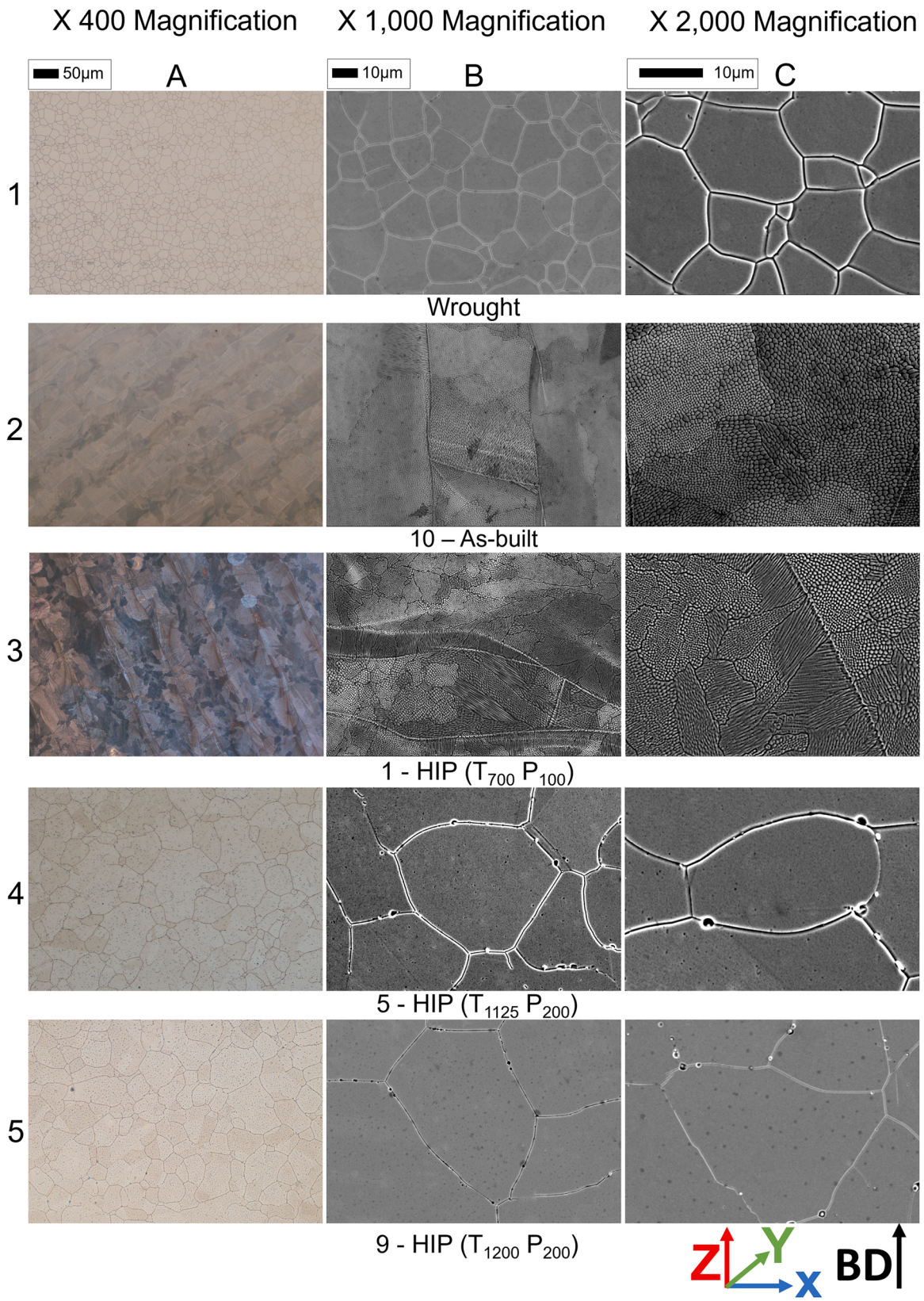


**Fig. 2.** Microstructures of X-Y plane, parallel to the build plate for wrought, conditions 10 - As-built, 1 - HIP ($T_{700}$ $P_{100}$), 5 - HIP ($T_{1125}$ $P_{137}$) and 9 - HIP ($T_{1200}$ $P_{200}$).

## 3. Results and discussion

### 3.1. Density and microscopy

The mean measured density for parts produced prior to post-production treatment was 7.94 ± 0.06 g $cm^{-3}$, equivalent to 99.26 % of the density of wrought 316L. The population variance of these results is 3.691 × $10^{-6}$ $g^2$ $cm^{-6}$ with a population standard deviation of 6.015 × $10^{-3}$. Post treatment, the mean measured density was 7.95 ± 0.07 g $cm^{-3}$, equivalent to 99.40 % of the density of wrought 316L. The microstructures of the X-Y plane for each of the heat-treated variants, as compared to the wrought equivalent, are displayed in Figs. 2 and 3. The microstructures and grain sizes displayed are representative of each temperature point due to minimal variation in these quantities across different pressure points. Each post-production treatment resulted in an increase to the measured density of parts with treatment 1 - HIP ($T_{700}$ $P_{100}$) producing the highest measured density of (7.97 ± 0.0) g $cm^{-3}$, equivalent to 99.63 %. However, treatment 8 - HIP ($T_{1125}$ $P_{200}$) produced the largest increase in density with an increase of 0.45 %. This value however is not vastly different from the mean percentage increase. This suggests that whilst there are variations in the density improvement across cycles, these variations are not significant to justify selecting a treatment based on the measured density alone. This may be due to the lowest pressure variable used in this work being above the threshold pressure, above which increasing the pressure further does not improve the HIP cycles' ability to remove porosity.

The wrought condition, as shown in Fig. 2 locations 1A, 1B and 1C, demonstrates an equiaxed grain structure with no preferential directionality in grain growth. In contrast, treatment 10 - as-built, as given in Fig. 2, locations 2A, 2B and 2C, demonstrates a typical LPBF microstructure with large melt pools and melt pool boundaries that can be clearly observed. At higher magnifications (Fig. 2 locations 2B and 2C), a sub grain cellular structure is also visible [33]. These cellular structures are less than 1 μm in length and form due to the high cooling rates experienced in the LPBF process, promoting the growth of columnar grain structures in an epitaxial manner, perpendicularly to the build plate [34]. It has been reported elsewhere in the literature that in conditions similar to the low temperature HIP cycle used in this research that these sub-cellular structures are the feature of elemental contrast and are not preserved at the low temperature HIP condition seen here [35]. However, work presented by Reijonen et al. shows the preservation of these cells at a HIP temperature of 1150 °C and a pressure of 100 MPa for four hours [36]. At shorter durations at increased temperatures, these cellular structures have been shown to be unaffected by heat treatment at 700 °C whilst becoming thinner and diffuse at 800 °C, with full removal observed at 900 °C [37–40]. The microstructure of treatment conditions 1 - HIP ($T_{700}$ $P_{100}$), 4 - HIP ($T_{700}$ $P_{137}$) and 7 - HIP ($T_{700}$ $P_{200}$), which refer to the low temperature treatment, are effectively identical to the as-built microstructure with the same key features being identifiable in representative images of low temperature treatment in Fig. 2 locations 3A, 3B and 3C.

The mid temperature treated samples, 2 - HIP ($T_{1125}$ $P_{100}$), 5 - HIP ($T_{1125}$ $P_{137}$) and 8 - HIP ($T_{1125}$ $P_{200}$) as given in Fig. 2 locations 4A, 4B and 4C, do not display obvious melt pools or melt pool boundaries, however it is possible to see some remnants of this structure in Fig. 2, location 4A where larger grains run parallel to each other, surrounded by smaller grains. The sub grain cellular structure however has been removed entirely and is not visible at higher magnifications (as seen in Fig. 2, 4B and C).

The high temperature treated samples, 3 - HIP ($T_{1200}$ $P_{100}$), 6 - HIP ($T_{1200}$ $P_{137}$) and 9 - HIP ($T_{1200}$ $P_{200}$) as displayed in Fig. 2 locations 5A, 5B and 5C, have a noticeably larger grain size than the low and mid temperature treated samples, along with a more equiaxed microstructure. The melt pools, melt pool boundary and sub grain cellular features have been removed entirely and overall, the microstructures of the high temperature treated samples resemble that of the wrought sample in this respect. The grain size of the high temperature sample however is larger than the wrought sample. The microstructure of sample 11 - HIP ($T_{1125}$ $P_{200}$ - long hold), representing the long hold treatment, is portrayed in Fig. 3. The images show that this treatment produced the largest measured grain size and does not contain any of the AM microstructural associated features as discussed previously. The measured grain sizes for each of these heat-treated variants are displayed in ascending order in Fig. 4, together with their respective standard deviations. The low variance and standard deviation of measured densities pre-treatment suggests that the build parameters selected produced parts of consistent density. The conditions in HIP processing drive local deformation and promotes recrystallisation, resulting in coarser and more equiaxed grains. This produces a microstructure similar to that of wrought 316L as visible in Fig. 2 (locations 1,4,5 a,b and c) and in Fig. 3 [38,41]. Increasing the temperature, pressure or the time setpoints of the HIP process drives these effects even further and increases the chances of complete recrystallisation occurring. This aligns with the complete recrystallisation and largest grain size measurements in this work obtained from condition 11 - HIP ($T_{1125}$ $P_{200}$ - long hold).

The results obtained from microscopy are logical in that the samples with the largest grain sizes were those subjected to the highest absolute temperature allowing for faster diffusion and thus grain growth. Additionally, these samples spent the longest time at an increased temperature due to the constant ramp rate used in the HIP cycles. The error associated with the grain size measurements of samples from treatment 9 - HIP ($T_{1200}$ $P_{200}$) and the long hold treatment 11 - HIP ($T_{1125}$ $P_{200}$ - long hold) have the largest variation across the conditions. The microstructures displayed in Fig. 3 can be seen to have a large variation in

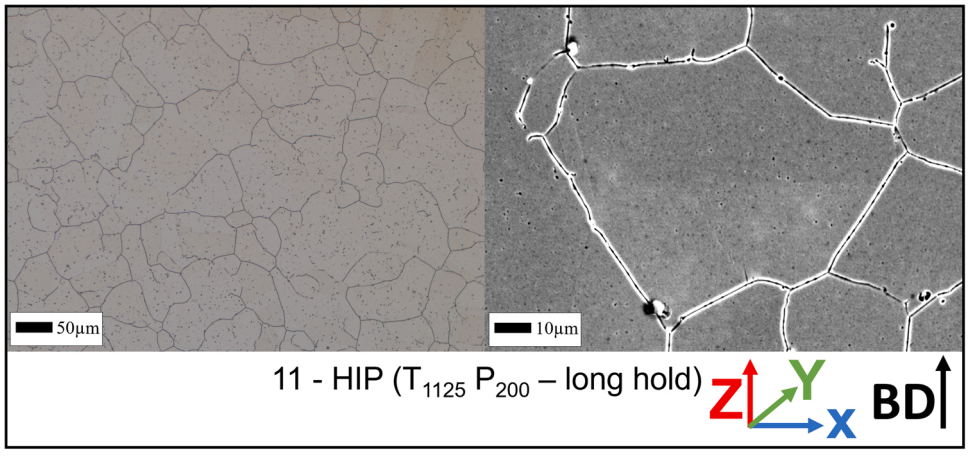


**Fig. 3.** Microstructures of X-Y plane, parallel to the build plate for condition 11 - HIP ($T_{1125}$ $P_{200}$ - long hold).

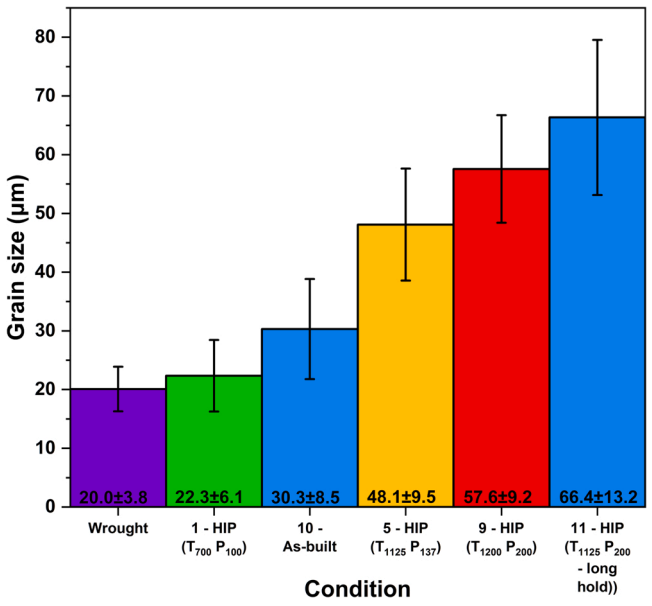


**Fig. 4.** Mean grain sizes of samples from the different variants. Error bars indicate the respective standard deviation values. Green represents low, amber represents medium and red represents high HIP temperature setpoints, respectively. Conditions 10 and 11 are displayed in blue and the wrought equivalent is presented as purple.

grain size. This is confirmed by the grain size measurements shown in Fig. 4 where condition 11 - HIP ($T_{1125}$ $P_{200}$ - long hold) has the largest variation in grain size. A study on the effect of heat treatment on the microstructure of selective layer melted 304 L stainless steel presented by Yang et al. has scatter bars that show a trend aligning with that presented in this work using a 2-hour treatment time [42]. There is a pronounced higher scatter of the heat-treated samples above 700 °C, with increasing standard deviation for higher annealing temperatures. There are bimodal features visible in the microstructures of conditions 9 - HIP ($T_{1200}$ $P_{200}$) and 11 - HIP ($T_{1125}$ $P_{200}$ - long hold) in Figs. 1 and 2 respectively comprising of large and significantly smaller grains. This accounts for the large variation in grain size associated with these conditions. Work published by Higgins et al. examines the effects of grain growth on microstructures with sub grain structures and non-uniform dislocations/stored energy similar to that in materials prepared by laser powder bed fusion. They detail a bimodal microstructure was observed comprising of noticeably larger and smaller grains similar to that present in conditions 9 - HIP ($T_{1200}$ $P_{200}$) and 11 - HIP ($T_{1125}$ $P_{200}$ - long hold) [43].

The microstructure of the samples subjected to the mid temperature HIP cycles, which correspond to the HIP temperature used, similarly do not display melt pools or melt pool boundaries. This directionality is completely removed in the high temperature 9 - HIP ($T_{1200}$ $P_{200}$) and long hold 11 - HIP ($T_{1125}$ $P_{200}$ - long hold) conditions. Therefore, it is suggested that these AM features are removed through the application of increased temperature treatment or increased time under heat treatment as the samples undergo microstructural coarsening. This is in agreement with Elangeswaran et al. [33]. The sub grain cellular structure which is common in AM materials is seemingly visible at higher magnifications within the as-built and low temperature treated samples, but is removed from all others. Subsequently it is possible to separate microstructures into one group which retains the melt pool, melt pool boundary and the visual cellular features of the as-built parts (conditions 1 - HIP ($T_{700}$ $P_{100}$), 4 - HIP ($T_{700}$ $P_{137}$), 7 - HIP ($T_{700}$ $P_{200}$) and 10 - ss-built), followed by another group wherein these features are removed, which accounts for the collection of remaining conditions.

### 3.2. Hardness and tensile

The hardness results as summarised in Table 5 indicate that the 10 - as-built condition and samples treated at the lowest HIP (700 °C) temperature point have the highest hardness, with values ranging from 215 to 234 HV, an increase of ~29 % compared to wrought. This coincides with these conditions also exhibiting amongst the smallest grain sizes as shown in Fig. 4. Aside from those outliers each of the conditions demonstrates a hardness within 8 % of the wrought value of 163.3 HV as measured in this work which is within the tolerance of the hardness tester.

Table 5 also contains the properties generated from tensile testing, with the most representative curves for each treatment displayed in Fig. 5. The mean surface roughness value across all tensile specimens was 8.68 µm with a population variance of 0.36 $(\mu m)^2$ (Table 3). The results for the HIP treated samples are separated into two distinct groups. Group A represents the samples treated at the lowest HIP temperature, conditions 1 - HIP ($T_{700}$ $P_{100}$), 4 - HIP ($T_{700}$ $P_{137}$) and 7 - HIP ($T_{700}$ $P_{200}$). Group B represents the remaining collection of treated samples. The group A samples, have increased ultimate tensile strength ($\sigma_{UTS}$) and yield strength ($\sigma_{YS}$) properties, exhibiting mean values of 584 MPa and 409 MPa respectively. However, their fracture elongation (*El*) values are reduced compared to the wrought value (60 %) [44] with a mean value of 47.8 %. The remaining treated samples, group B, all demonstrated an *El* value comparative to the wrought value (60 %) with an average *El* value of 59.0 %. However, the group B samples exhibit a decrease in $\sigma_{UTS}$ with a mean value of 542 MPa compared to the wrought value of 560 MPa [44]. Group B samples also suffered from a decrease in $\sigma_{YS}$ and fracture strength ($\sigma_f$) properties compared to Group A samples. Whilst there are variations in the data which could be linked to changes in the HIP treatment pressure, the significance of these effects is not dominant. Furthermore, it is possible to separate the data into two further groups from A and B respectively. As compared to group A, the as-built samples achieved a higher $\sigma$ value whilst in the elastic region (~510 MPa) compared to samples 1 - HIP ($T_{700}$ $P_{100}$), 4 - HIP ($T_{700}$ $P_{137}$) and 7 - HIP ($T_{700}$ $P_{200}$) (~440 MPa). Within group B a similar trend exists where the samples that were treated at the high temperature point and the long hold samples (3 - HIP ($T_{1200}$ $P_{100}$), 6 - HIP ($T_{1200}$ $P_{137}$), 9 -

**Table 5**
Measured Vickers hardness and tensile properties alongside their standard deviations.

| Condition | Hardness (HV) | *El* (%) | $\sigma_{UTS}$ (MPa) | $\sigma_{YS}$ (MPa) | $\sigma_f$ (MPa) |
|---|---|---|---|---|---|
| Wrought – tensile values taken from literature | 163.3 ± 4.2 | 60 [44] | 515 [44] | 205 [44] | – |
| 1 - HIP ($T_{700}$ $P_{100}$) | 215.7 ± 6.3 | 48.0 ± 1.1 | 582.7 ± 3.2 | 396.6 ± 5.9 | 463.3 ± 7.4 |
| 2 - HIP ($T_{1125}$ $P_{100}$) | 166.2 ± 7.3 | 58.0 ± 0.8 | 538.8 ± 3.9 | 304.6 ± 6.6 | 444.8 ± 5.4 |
| 3 - HIP ($T_{1200}$ $P_{100}$) | 149.9 ± 5.2 | 58.8 ± 0.7 | 535.8 ± 5.6 | 228.3 ± 4.1 | 445.9 ± 9.8 |
| 4 - HIP ($T_{700}$ $P_{137}$) | 223.3 ± 6.7 | 47.2 ± 1.0 | 585.3 ± 0.8 | 398.2 ± 2.0 | 475.6 ± 2.9 |
| 5 - HIP ($T_{1125}$ $P_{137}$) | 162.7 ± 6.5 | 57.5 ± 0.7 | 554.4 ± 1.9 | 296.0 ± 10.6 | 446.9 ± 6.3 |
| 6 - HIP ($T_{1200}$ $P_{137}$) | 163.5 ± 3.2 | 59.7 ± 0.4 | 541.7 ± 0.9 | 272.1 ± 4.5 | 441.1 ± 6.5 |
| 7 - HIP ($T_{700}$ $P_{200}$) | 214.9 ± 7.2 | 48.1 ± 0.1 | 585.1 ± 5.9 | 428.3 ± 4.8 | 449.5 ± 13.4 |
| 8 - HIP ($T_{1125}$ $P_{200}$) | 162.2 ± 5.5 | 59.7 ± 2.2 | 549.8 ± 5.7 | 294.6 ± 2.1 | 455.7 ± 3.6 |
| 9 - HIP ($T_{1200}$ $P_{200}$) | 154.8 ± 4.2 | 60.1 ± 0.5 | 530.8 ± 4.9 | 230.6 ± 4.1 | 442.6 ± 16.6 |
| 10 - As-built | 233.6 ± 8.2 | 48.0 ± 0.7 | 588.2 ± 4.2 | 474.3 ± 12.3 | 452.6 ± 7.9 |
| 11 - HIP ($T_{1125}$ $P_{200}$ - long hold) | 154.7 ± 2.9 | 59.5 ± 0.9 | 538.5 ± 2.5 | 221.9 ± 5.3 | 451.7 ± 16.5 |

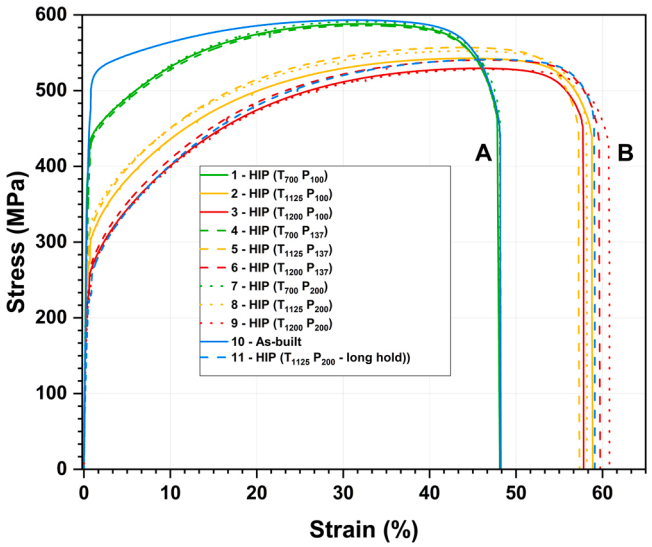


**Fig. 5.** Tensile results for each condition showing separation between samples with different microstructures induced by post processing treatment. Green represents low, amber represents medium and red represents high HIP temperature setpoints, respectively. Conditions 10 and 11 are displayed in blue. Solid, dash and dotted lines represent low medium and high pressure setpoints.

HIP ($T_{1200}$ $P_{200}$) and 11 - HIP ($T_{1125}$ $P_{200}$ - long hold)) exhibit a lower maximum $\sigma$ value in the elastic region compared to all other group B samples. Microstructurally, the difference between group A and B is the presence of the intrinsic AM features, the visibility of a sub-grain cellular structure, the presence of clearly visible melt pools and the anisotropy of the grains.

The results of the tensile testing reflect the measured grain sizes, generally following the standard Hall-Petch relationship [45]. The as-built condition samples demonstrate the highest measured hardness; this increased hardness compared to the wrought counterpart is common across AM materials. This is duly associated with the high cooling rates and complex thermal history resulting from the manufacturing process. The microstructures formed are comprised of a large fraction of highly misorientated low-angle grain boundaries (LAGBs) [46,47]. The dislocation tangled sub grain cellular walls also contribute to the increased hardness of the AM sample in the as-built state [38]. Dislocations in a polycrystalline aggregate can be categorised into geometrically necessary dislocations (GND) and statistically stored dislocations (SSD). GNDs are similarly aligned dislocations needed to accommodate for plastic bending in the material [38]. SSDs are stored by mutual random trapping during the material's manufacturing process [48]. With the process of recovery occurring as heat is added to the system during HIP treatments, GNDs migrate from cellular walls to more energetically-favourable regions such as sub grain boundaries. This occurs across each of the treatment temperature points and is a possible explanation for the decrease in hardness and tensile strength from 10-As-built to condition 1 - HIP ($T_{700}$ $P_{100}$) despite condition 10-As-built having a larger measured grain size. The densities of SSDs decrease more rapidly upon the addition of heat than GNDs due to their increased sensitivity to the release of thermal distortions formed in printing [38]. Increasing the time and temperature of treatment to the mid and high points in this work removed the inherent AM microstructural features and coarsened the grain structure. Further to this the dislocation density is modified as dislocations migrate throughout the microstructure and the density decreases as a whole but with a larger reduction in SSDs resulting in a decrease in overall hardness and significant softening effects [33,49].

The separation of the tensile data into two distinct groups aligns with the two groups reported in the microscopy and hardness findings. Conditions 1 - HIP ($T_{700}$ $P_{100}$), 4 - HIP ($T_{700}$ $P_{137}$), 7 - HIP ($T_{700}$ $P_{200}$) and 10 - as-built, whilst peaking at a higher $\sigma_{UTS}$ and attaining a higher $\sigma_{YS}$, suffered from fracture at a reduced *El* than all other conditions. This aligns with results documented in literature that found that as-built AM 316L components have demonstrated high strength but lower ductility than wrought components to various degrees, depending on the build parameters, build orientation and post-production treatments used [6,34]. In some work, the increased $\sigma_{UTS}$ and $\sigma_{YS}$ of the as-built condition was attributed to the microstructure being comprised of small grains with large misorientation angles, the density of which decreases with the addition of treatment temperatures similar to the mid and high setpoints used in this work [21]. The further differentiation of groups within this work is notable in that the tensile behaviour of the samples subjected to the high temperature HIP cycle is near identical to the behaviour of the long hold HIP cycle despite the long hold being carried out at the midpoint temperature. This suggests that for an application requiring a high level of ductility, then either a high temperature HIP cycle or a long hold at a lower temperature is advisable. The likelihood however is that the cost associated with a long hold is greater than that required for a higher temperature cycle and therefore the long hold is not recommended. In addition to this the mean *El* value achieved by the midpoint temperature treated parts (58.4 %) is comparable to the high temperature average (59.5 %) whilst maintaining a $\sigma_{YS}$ of 298.4 MPa compared to the high temperature average of 243.7 MPa. The significance of this is that for an application wherein a high elongation as well a high $\sigma_{YS}$ is required, this work suggests that the midpoint temperature and pressure HIP cycles are more favourable than HIP treating at the higher temperature point. The hardness and $\sigma_{UTS}$ values presented in Table 5 align with the well-known relationship wherein the ratio of Vickers hardness to $\sigma_{UTS}$ is derived to be approximately 3, and between 3.21 and 4.01 for AM 316L specifically, as presented by Kim [45,50].

Despite the mechanical properties generally following the standard Hall-Petch relationship, a modified Hall-Petch relationship is more applicable to AM 316L, as proposed by Cui et al. [38], which allows for the prediction of yield strength values using $\sigma_{YS} = \sigma_0 + \sigma_{GB} + \sigma_{SS} + \sigma_p + \sigma_{Dis}$. This accounts for a contribution from friction stress $\sigma_0 \sim 15$ (MPa) [51–53], $\sigma_{GBS} = k\sqrt{d}$ is the contribution from strain boundary strengthening, and $\sigma_{Dis} = M\alpha Gb\sqrt{\rho}$ is the contribution from dislocation strengthening. *M*, the orientation factor is taken as 2.20, α as 0.30, G, the shear modulus as 78 GPa, b the Burgers vector as $2.5 \times 10^{-10}$ m, *k* the Hall-Petch parameter is approximately 300 MPa $\mu m^{-0.5}$ and d being the average grain size 32.5 (μm) [38,54]. The contributions of precipitation hardening, $\sigma_p$, and solution strengthening, $\sigma_s$, are taken as 12.50 MPa and 96.60 MPa from Cui et al. [38]. Assuming that the dislocation density of 10 - as-built is $6 \times 1014$ $m^{-2}$ as per Bahl et al. [49], then the calculated yield strength for the as-built condition using the grain size measured in this work is 492 MPa. This value is in strong agreement with the value of 474.3 MPa ± 12.3 recorded in this work in Table 5.

Increased $\sigma_{YS}$ values have been attributed in literature to the fine granular structure and a high dislocation density present in as-built AM samples [55]. This correlates with the conclusions drawn from microstructural observations made in this work. For HIP cycle optimisation, assuming the same volume of gas is used per HIP cycle, ultimately the overall cost of the HIP cycle is determined by the treatment temperature and the length of cycle. The tensile results obtained in this work suggest that the high temperature treatments are only required for an application wherein attaining absolute maximum possible elongation is crucial. Samples containing melt pool, melt pool boundaries and visibly cellular microstructural features were found to result in increased performance in some of the tensile properties, however they also suffer from reduced fracture elongation. Additionally, the as-built sample has the marginally highest $\sigma_{UTS}$ and highest $\sigma_{YS}$ values, whilst condition 4 - HIP ($T_{700}$ $P_{137}$) produced the highest outright $\sigma_f$ value.

### 3.3. Fatigue properties

The mean surface roughness value across all fatigue specimens was

0.99 μm with a population variance of 0.0002 $(\mu m)^2$ (Table 4). In the samples subjected to the lower of the two maximum applied stress ($\sigma_{MAX}$) values (330 MPa), the as-built (condition 10) sample and those subjected to the low temperature conditions (1 - HIP ($T_{700}$ $P_{100}$), 4 - HIP ($T_{700}$ $P_{137}$) and 7 - HIP ($T_{700}$ $P_{200}$)) all reached the run-out limit and did not fail during testing. These variants also surpassed the fatigue life of the wrought stainless steel 316L equivalent (~40,000 cycles), with data generated in [56] and [57]. The samples from the remaining conditions all failed within the order of 10,000 cycles. In the higher $\sigma_{MAX}$ regime ($\sigma_{MAX}$ = 375 MPa), condition 4 - HIP ($T_{700}$ $P_{137}$) again reached the run-out condition, surpassing 100,000 fatigue cycles. 10 - as-built and condition 7 - HIP ($T_{700}$ $P_{200}$) were the next best performing samples, failing between 65,000 and 75,000 cycles. This was closely followed by condition 1 - HIP ($T_{700}$ $P_{100}$) which failed just under 48,000 cycles, all of which outperform the wrought variant (~20,000 cycles). The remaining conditions all failed within 2155 cycles. All the results are displayed in Table 6 and graphically illustrated in Fig. 6.

Post-test fractographic assessments of the fatigue samples revealed that cracking predominantly initiated at the surface of the gauge length and propagated towards the centre of the samples, thus indicating that the presence of any potential internal defective regions had minimal influence on the crack initiation life of these samples. Despite the compressive nature of the loading ratio (R = −1), fatigue striations are visible on several of the fracture surfaces, tracking perpendicularly to the growth direction of the crack. Some indicative examples of the observed fractures are presented in Fig. 7. This figure shows the fracture surfaces of samples from condition 9 - HIP ($T_{1200}$ $P_{200}$), which represents the high temperature, high pressure HIP condition, and condition 10 - as-built. These samples saw contrasting behaviours under fatigue loading, with condition 10 - as-built significantly outperforming condition 9 - HIP ($T_{1200}$ $P_{200}$), despite not being subjected to a post-process HIP cycle. Like that seen for the hardness and tensile results, this can be attributed to the smaller grain size observed in the X-Y plane in condition 10 - as-built material (32.49 μm), as compared to 58.07 μm in condition 9 - HIP ($T_{1200}$ $P_{200}$). Together with fractographic images displayed in Fig. 7a and b, where minimal evidence of any defective regions can be seen in the as-built condition, this clearly indicates that the as-built material already had a high degree of consolidation and the high temperature, high pressure HIP operation has predominantly only acted to promote grain growth in the material, to the detriment of the sample's hardness, tensile and fatigue performance.

The results of both the higher and lower stress regime fatigue tests align with the previous mechanical results wherein the as-built sample and those treated at low temperature tend to outperform the remaining conditions. Further performance differentiation between the low temperature HIP treated and as-built samples can be considered for the tests subjected to the lower $\sigma_{MAX}$ value (330 MPa). Since the condition 4 - HIP ($T_{700}$ $P_{137}$)'s sample reached the run-out limit, the failure point is unknown making it difficult to estimate the full potential fatigue life of this sample. Whilst unmelted powder and inclusions contribute to a higher defect volume and subsequently a shorter fatigue life, the high ductility of 316L lends to its fatigue performance being influenced heavily by the material's microstructure [30]. It has been shown that retention at high temperatures and slow cooling rates have led to a high reduction of dislocation density, the removal of sub grain cellular structures and subsequently, reduced strength in AM 316L [44]. This is in agreement with the results presented in this work wherein the fatigue performance aligns with the differences in microstructures between the samples and pore-induced failure is not observed in the fracture surface of any sample. This work indicates that a sweet spot in HIP treatment pressure exists for fatigue performance in 316L which lies between the lower (100 MPa) and the higher (200 MPa) pressure thresholds.

The fatigue results presented are from one test performed under each condition and provide an indication of the expected fatigue behaviour. However, care must be taken when making conclusions from the gathered results as they have limited statistical meaning.

**Table 6**
Fatigue test results across the two stress regimes for each treatment.

| Condition | $\sigma_{MAX}$ (MPa) | $N_f$ | $\sigma_{MAX}$ (MPa) | $N_f$ |
|---|---|---|---|---|
| 1 - HIP ($T_{700}$ $P_{100}$) | 330 | 100,000 | 375 | 47,911 |
| 2 - HIP ($T_{1125}$ $P_{100}$) | 330 | 5674 | 375 | 699 |
| 3 - HIP ($T_{1200}$ $P_{100}$) | 330 | 4807 | 375 | 1297 |
| 4 - HIP ($T_{700}$ $P_{137}$) | 330 | 100,000 | 375 | 100,000 |
| 5 - HIP ($T_{1125}$ $P_{137}$) | 330 | 5936 | 375 | 1428 |
| 6 - HIP ($T_{1200}$ $P_{137}$) | 330 | 4446 | 375 | 2155 |
| 7 - HIP ($T_{700}$ $P_{200}$) | 330 | 100,000 | 375 | 66,761 |
| 8 - HIP ($T_{1125}$ $P_{200}$) | 330 | 2136 | 375 | 1507 |
| 9 - HIP ($T_{1200}$ $P_{200}$) | 330 | 1720 | 375 | 1382 |
| 10 - As-built | 330 | 100,000 | 375 | 74,064 |
| 11 - HIP ($T_{1125}$ $P_{200}$ - long hold) | 330 | 8238 | 375 | 1380 |
| Wrought (data from [56,57]) | 330 | 40,000 | 375 | 20,000 |

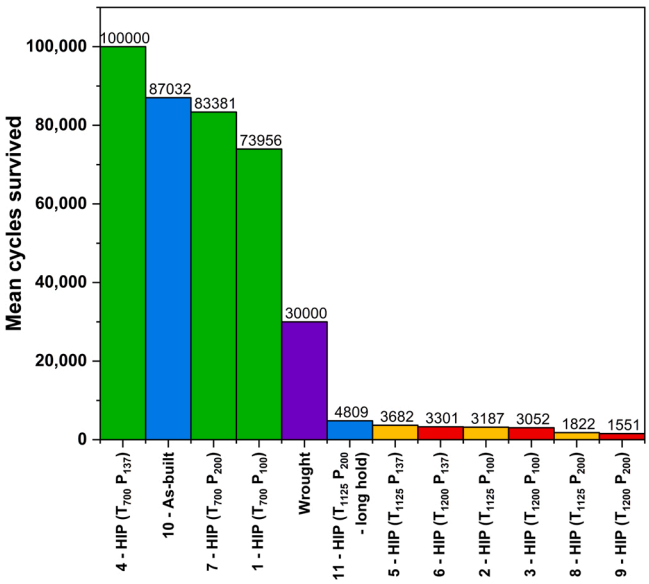


**Fig. 6.** Mean cycles survived by the 316L variants during fatigue testing. The colours green, amber and red represent low, medium and high temperature setpoints. Conditions 10,11 are plotted in blue and the wrought equivalent is presented as purple.

### 3.4. Pitting corrosion

A potentiodynamic curve recorded on samples from conditions 1 - HIP ($T_{700}$ $P_{100}$) and 2 - HIP ($T_{1125}$ $P_{100}$) are displayed in Fig. 8. The pitting potential refers to the potential at which pits become active and autocatalytic. The repassivation potential refers to the potential on the downward scan at which point aggressive ions within the pit are replaced by a passive layer which prevents further pit growth. This point is defined as the region of the potentiodynamic curve wherein the reverse potential crosses the forward potential. The repassivation and pitting potentials have been highlighted and arrows have been superimposed on the curves to indicate the scan direction. In the examples shown, condition 1 - HIP ($T_{700}$ $P_{100}$) demonstrates repassivation and an increased pitting potential relative to condition 2 - HIP ($T_{1125}$ $P_{100}$) which did not repassivate. The horizontal lines visible between 0.4 and 0.5 V for condition 2 - HIP ($T_{1125}$ $P_{100}$) are representative of metastable pits which form and then re-passivate without maturing to fully sized active pits [58]. The results of the corrosion testing are plotted in Fig. 10. The wrought samples demonstrated a pitting potential of 0.576 ± 0.007 V rel. SCE. The pitting potential of the as-built parts was 0.613 ± 0.389 V rel. SCE, representing a pitting potential close to the wrought

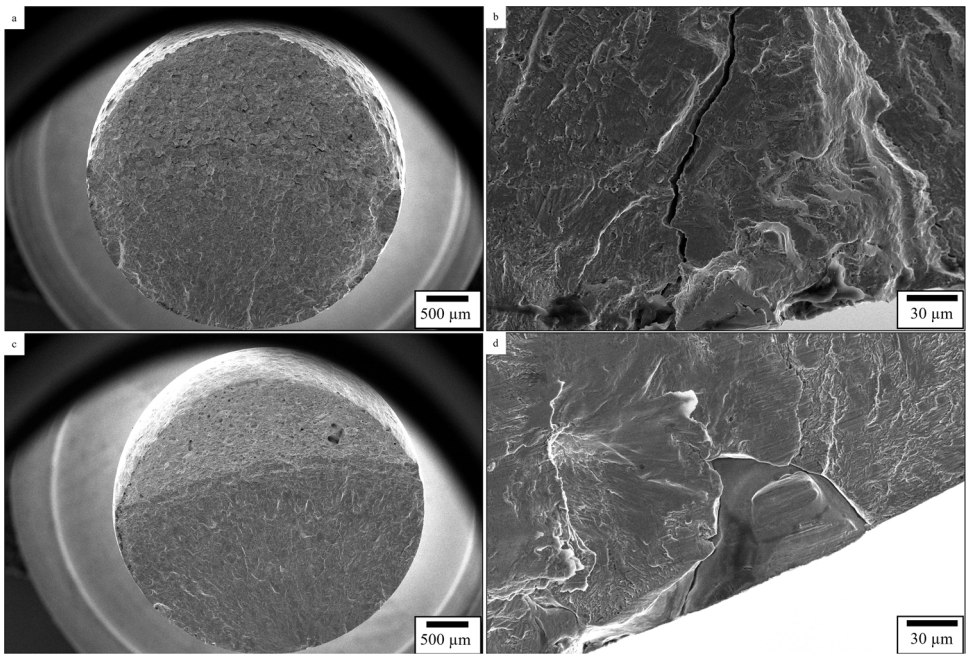


**Fig. 7.** SEM fractographic images of Treatment 9 - HIP ($T_{1200}$ $P_{200}$) at **a.** low and **b.** high magnification. Images of 10 - As-built at **c.** low and **d.** high magnification.

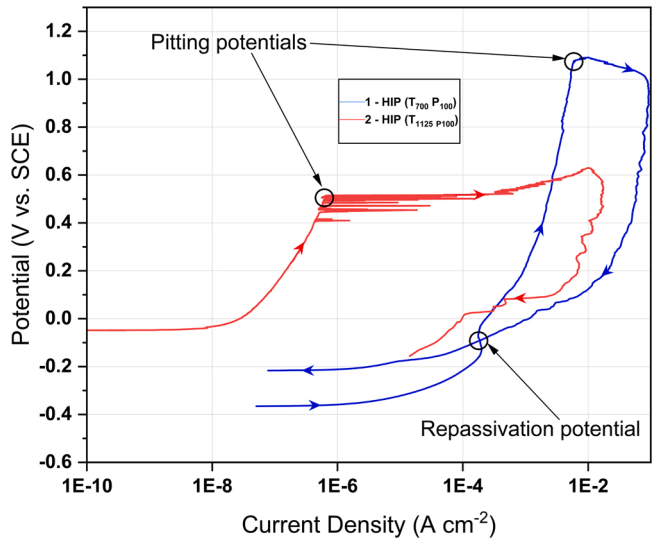


**Fig. 8.** Potentiodynamic curves of samples from conditions 1 - HIP ($T_{700}$ $P_{100}$) and 2 - HIP ($T_{1125}$ $P_{100}$) with key points labelled and arrows indicating the scan direction.

value but with a larger associated error. The condition with the highest recorded pitting potentials was condition 1 - HIP ($T_{700}$ $P_{100}$) with a mean pitting potential of 1.010 ± 0.058 V rel. SCE, an increase in pitting potential of 75 % relative to wrought. The variation in recorded values varies significantly in the AM parts in comparison to the extremely small variation reported in the wrought counterpart. Repassivation was recorded in each of the experiments carried out on the wrought parts at a mean value of − 0.103 ± 0.002 V. Repassivation was recorded for all repeats on samples from conditions 3 - HIP ($T_{1200}$ $P_{100}$), 8 - HIP ($T_{1125}$ $P_{200}$) and 10 - as-built, with mean values of − 0.274 ± 0.110, − 0.261 ± 0.108, 0.130 ± 0.474.

Interpreting the corrosion data is non-trivial as although having the highest possible pitting and repassivation potentials are preferential, the variability of results is equally important. This importance is due to the severe effect that pitting corrosion has on the structural integrity of a sample. Pitting corrosion can lead to the onset of stress corrosion cracking which can lead to the sudden failure of normally ductile alloys when subjected to tensile stresses. The ideal combination of parameters being a high pitting and repassivation potential each with a low degree of variation. This combination of parameters is only achieved by the wrought part. Despite condition 1 - HIP ($T_{700}$ $P_{100}$) producing a sample with the highest measured pitting potential across all tests with comparatively low variation to the other AM samples, the variance in pitting potential is larger than that of the wrought part. Collectively the

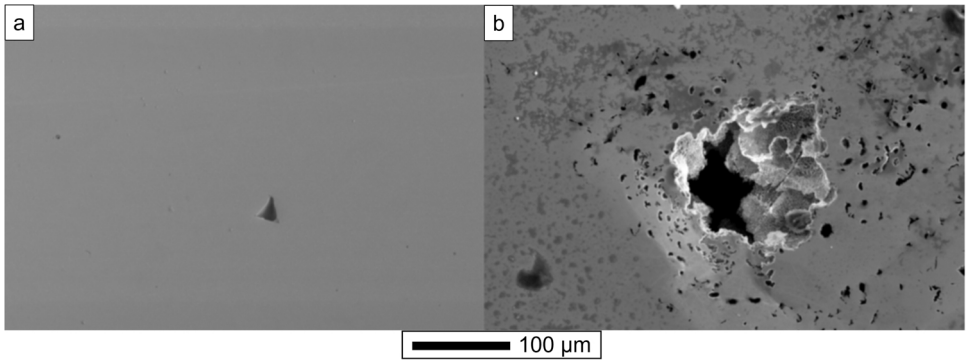


**Fig. 9.** Scanning electron micrograph at 200x of a porosity feature a) pre and b) post localised corrosion attack on a sample from condition 4 - HIP ($T_{700}$ $P_{137}$).

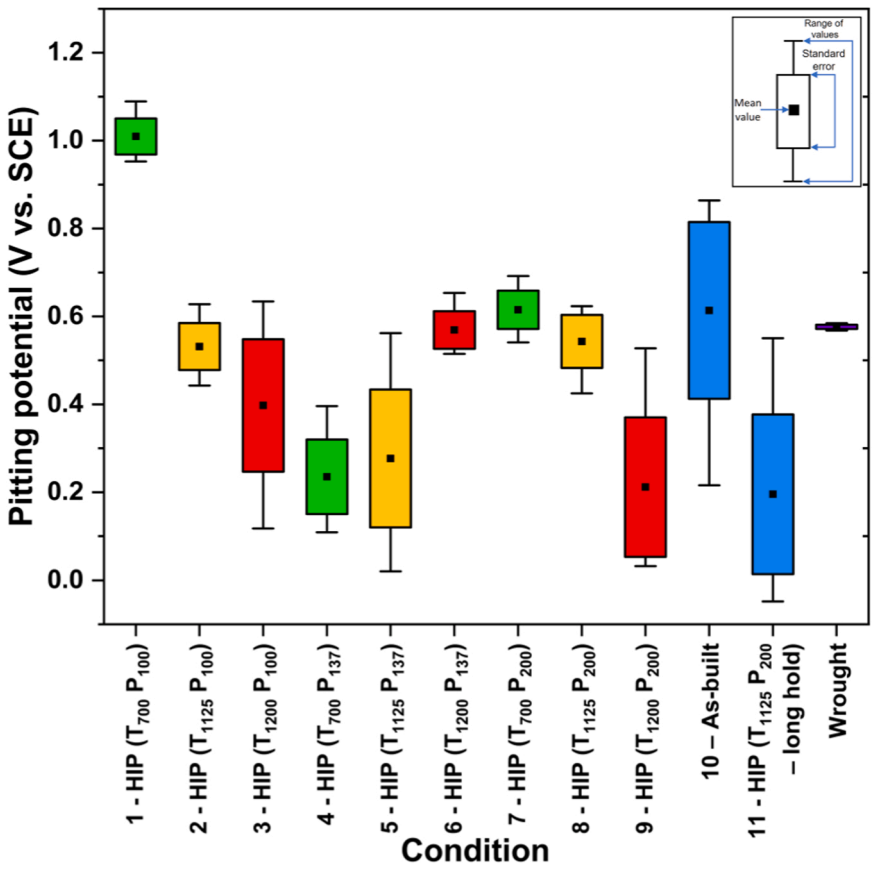


**Fig. 10.** Recorded pitting potentials for the different 316L variants. The colours green, amber and red represent low, medium and high temperature setpoints. Conditions 10,11 are plotted in blue and the wrought equivalent is presented as purple.

mean standard deviation associated with the treated AM samples (all samples across all conditions excluding wrought and as-built) pitting potentials was 0.135 V compared to 0.284 V for the as-built parts and 0.007 V for the wrought parts. This indicates that the porosity reducing effects of the HIP treatments succeeded in reducing the spread of the pitting potentials by 52.46 %. Despite this, samples from condition 1 - HIP ($T_{700}$ $P_{100}$) failed to repassivate in two of its tests despite recording the highest average pitting potential. Conversely whilst samples from conditions 3, 8 and 10 achieved repassivation in each of their tests, the variation associated with the repassivation potentials was significantly increased compared to wrought. Further to this, the pitting potentials recorded by samples from conditions 3 - HIP ($T_{1200}$ $P_{100}$), 8 - HIP ($T_{1125}$ $P_{200}$) and 10 - as-built have large variations. The pitting performance of wrought 316L was determined by subjecting the traditional variant to the same conditions as the LPBF material tested in this work. The response of the wrought material was determined by the uniformity of the grains as well as the density of high angle grain boundaries. It has been previously found that more uniform microstructures with larger grains and a lower grain boundary density show improved pitting performance [59,60]. Despite the effect that the microstructure has on the mechanical properties investigated in this work, the pitting corrosion performance of the parts is not significantly affected by the presence of these microstructural features. This is due to the fact that any small irregularity in the surface of the material including small spherical porosity and larger irregularly shaped porosity features can act as initiation sites for localised pitting corrosion [61,62]. This is displayed in Fig. 9 where localised corrosion initiated preferentially at an irregularly shaped pore. This pore measured approximately 22 μm in width prior to localised corrosion attack which increased to 156 μm after corroding. Irregularly shaped porosity at melt pool boundaries can lead to pits forming in unconventional shapes, which can be attributed to the electrochemical reaction evolving along cellular structures that typically have a higher dislocation density than within the melt pool [63]. Further to this, porosity with semi-occluded regions are conducive to facilitating localised corrosion through differential aeration due to the restricted diffusion of oxygen into these regions, as per the Fontana Greene mechanism of crevice corrosion [64]. Further application of these mechanisms infers that a smaller porosity region which is semi occluded may induce pitting at a lower potential than a larger porosity feature that is not semi occluded, suggesting that the morphology and geometry of porosity on the samples' surface influences the localised pitting behaviour more so than the overall bulk porosity.

This suggests that the pitting performance of AM parts is dependent on the level of porosity and whilst HIP treatments, as shown in this work, are able to reduce the presence of porosity, lower levels of porosity are typically necessary to facilitate a pitting performance comparable or superior to wrought 316L. Therefore, whilst the performance of some samples in some aspects of the pitting performance have performed superiorly to wrought 316L, the large variation associated with the corrosion results reduces the confidence in the performance of the AM parts in corrosive environments. Selectively identifying an area to test that is free from any porosity may result in a pitting performance that is comparable or improved when compared to wrought parts, however this is not representative of the material in situ. Whilst microstructural features can determine the corrosion performance of materials, microscopic variations at the surface appear to be the dominant feature.

### 3.5. Closing statement

Whilst the post processing conditions investigated in this work did not entirely remove porosity from the LPBF variants, some porosity was eliminated, and the treatments were shown to have noticeable impact on

both mechanical and pitting potential properties. Post-processing HIP cycles at mid (1125 °C) and high (1200 °C) temperatures remove the melt pools, melt pool boundaries and sub-grain cellular features that are present in the microstructure from the additive process. Such treatments also promoted grain growth which led to a reduction in the tensile strength (UTS 588 MPa in condition 10 - as-built to 533 MPa in condition 9 - HIP (T1200 P200)), hardness (233 HV condition 10 - as-built to 154 HV condition 9 - HIP (T1200 P200)) and fatigue properties of the material, but fracture elongation and ductility were seen to increase. Variations in pressure did not induce a significant difference in tensile properties. In terms of mechanical properties, condition 4 - HIP ($T_{700}$ $P_{137}$) reached the run-out limit for each of the fatigue tests, whilst also having higher hardness, ultimate tensile strength and fracture stress than most of the other conditions. The samples subjected to condition 4 - HIP (T700 P137) do not have enlarged grain boundaries, whilst density has been increased by the HIP treatment. This suggests that in terms of fatigue performance, condition 4 - HIP ($T_{700}$ $P_{137}$) can be considered the optimal HIP cycle. Increasing the hold time of the HIP cycle resulted in no significant improvement in any of the metrics quantified in this work. The overarching conclusion from the results across all tests as outlined in this article are that the microstructural features of the material are highly dependent on the post processing treatment chosen. These microstructural features significantly impact the performance of the material in the mechanical testing carried out. Whilst these microstructural variations can influence the corrosion pitting performance of the microstructure of the material, porosity features at the surface of the material are the main contributing factors to the overall pitting performance of the alloy. The performance of the as-built sample highlights the importance of optimising HIP parameters. Running a HIP cycle at the optimum temperature but at a non-optimum pressure can result in a decrease in fatigue performance due to microstructural grain growth, whereas treating at the optimum temperature and pressure results in an increased fatigue performance compared to the as-built variant.

## 4. Conclusions

The main goal of this research was to identify the optimal hot isostatic pressing parameters to enhance the mechanical and corrosion properties of laser powder bed fused stainless steel 316L. From this work, the following conclusions can be drawn:

- Post-processing HIP cycles at mid (1125 °C) and high (1200 °C) temperatures remove the melt pools, melt pool boundaries and sub-grain cellular features that are present in the microstructure from the additive process.
- The post-process HIP cycle at the lowest of the temperatures (700 °C) was found to result in an increased yield strength and a reduced elongation to fracture compared to other treatments.
- Condition 4 - HIP ($T_{700}$ $P_{137}$) was seen to have the highest $N_f$ at the higher stress value, whilst being intermediate on ultimate tensile strength and recording the lowest average pitting potential.
- Samples from condition 1 - HIP ($T_{700}$ $P_{100}$) produced the highest mean pitting potential with a value of 1.010 ± 0.058 V rel. SCE, an increase in pitting potential of 75 % relative to the wrought value of 0.576 ± 0.007 V rel. SCE.
- HIP treatments succeeded in reducing the spread of the pitting potentials by 52.46 % compared to as-built parts. Considering the pitting and repassivation potentials and their associated errors, none of the AM samples tested performed as well as the wrought sample across all metrics.

## CRediT authorship contribution statement

**N.P. Lavery**: Writing – review & editing, Supervision, Resources, Formal analysis, Data curation, Conceptualization. **J.H. Sullivan:** Writing – review & editing, Supervision, Resources, Funding acquisition, Formal analysis, Conceptualization. **Iwan Salvu Grech:** Writing – review & editing, Writing – original draft, Visualization, Validation, Software, Methodology, Investigation, Formal analysis, Data curation. **J. Plummer:** Resources. **R.J. Lancaster:** Writing – review & editing, Resources, Formal analysis, Data curation.

## Declaration of Competing Interest

The authors declare that they have no known competing financial interests or personal relationships that could have appeared to influence the work reported in this paper.

## Data Availability

The data that has been used is confidential.

## Acknowledgements

This work was funded by the Defence Science and Technology Lab (DSTL) Project code: DSTLX1000128518. The use of the MACH1 laboratories and the Advanced Imaging of Materials (AIM) facilities at Swansea University are gratefully acknowledged.

## References

[1] D. Peckner, I.M. Bernstein, Handbook of Stainless Steels, McGraw-Hill Book Company, New York, 1977.
[2] M. Dzemko, B. Engelmann, J. Hartmann, J. Schmitt, Toward shifted production strategies through additive manufacturing: a technology and market review for changing value chains, Procedia CIRP 86 (2019) 228–233, no. ISSN 2212-8271.
[3] C.Y. Yap, C.K. Chua, Z.L. Dong, Z.H. Liu, L.E. Loh, S.L. Sing, Review of selective laser melting: materials and applications, Appl. Phys. Rev. 2 (4) (2015).
[4] A. Sola, A. Nouri, Microstructural porosity in additive manufacturing: the formation and detection of pores in metal parts fabricated by powder bed fusion, J. Adv. Manuf. Process. 1 (3) (2019).
[5] H. Gong, K. Rafi, H. Gu, T. Starr, B. Stucker, Analysis of defect generation in Ti-6Al-4V parts made using powder bed fusion additive manufacturing processes, Addit. Manuf. 1–4 (2014) 89–98.
[6] N. Lavery, J. Cherry, S. Mehmood, H. Davies, B. Girling, E. Sackett, S.G. Brown, J. Sienz, Effects of hot isostatic pressing on the elastic modulus and tensile properties of 316L parts made by powder bed laser fusion, Mater. Sci. Eng. 693 (2017) 186–213.
[7] S. Dryepondt, P. Nandwana, P. Fernandez-Zelaia, F. List, Microstructure and high temperature tensile properties of 316L fabricated by laser powder-bed fusion, Addit. Manuf. 37 (101723) (2021).
[8] P. Dong, F. Vecchiato, Z. Yang, M. Wenman, The effect of build direction and heat treatment on atmospheric stress corrosion cracking of laser powder bed fusion 316L austenitic stainless steel, Addit. Manuf. 40 (101902) (2021).
[9] N.S. Al-Mamun, K.M. Deen, W. Haider, E. Asselin, I. Shabib, Corrosion behavior and biocompatibility of additively manufactured 316L stainless steel in a physiological environment: the effect of citrate ions, Addit. Manuf. 34 (101237) (2020).
[10] A.M. Roach, B.C. White, A. Garland, B.H. Jared, J.D. Carroll, L.B. Boyce, Size-dependent stochastic tensile properties in additively manufactured 316L stainless steel, Addit. Manuf. 32 (101090) (2020).
[11] C. Pauzon, E. Hryha, P. Forêt, L. Nyborg, Effect of argon and nitrogen atmospheres on the properties of stainless steel 316 L parts produced by laser-powder bed fusion, Mater. Des. 179 (107873) (2019).
[12] A. Aversa, A. Saboori, E. Librera, d M. Chirico, S. Bianmino, M. Lombardi, P. Fino, The role of Directed Energy Deposition atmosphere mode on the microstructure and mechanical properties of 316L samples, Addit. Manuf. 34 (101274) (2020).
[13] J. Boes, A. Röttger, L. Becker, W. Theisen, Processing of gas-nitrided AISI 316L steel powder by laser powder bed fusion – microstructure and properties, Addit. Manuf. 30 (100836) (2019).
[14] E.H. Valente, V.K. Nadimpalli, S.A. Andersen, D.B. Pederson, T.L. Christiansen and M.A.J. Somers, fusion, Influence of atmosphere on microstructure and nitrogen content in AISI 316L fabricated by laserbased powder bed, in: Proceedings of the 19th International Conference and Exhibition (EUSPEN 2019), Bilbao, 2019.
[15] A. Röttger, K. Geenen, M. Windmann, F. Binner, W. Theisen, Comparison of microstructure and mechanical properties of 316 L austenitic steel processed by selective laser melting with hot-isostatic pressed and cast material, Mater. Sci. Eng.: A 678 (2016) 365–376.
[16] C. Pauzon, A. Leicht, U. Klement, P. Forêt, E. Hryha, Effect of the process gas and scan speed on the properties and productivity of thin 316L structures produced by laser-powder bed fusion, Metall. Mater. Trans. A 51 (2020) 5339–5350.
[17] H.V. Atkinson, S. Davies, Fundamental aspects of hot isostatic pressing: an overview, Met. Mater. Trans. A 31 (12) (2000) 2981–3000.

[18] A. du Plessis, E. Macdonald, Hot isostatic pressing in metal additive manufacturing: X-ray tomography reveals details of pore closure, Addit. Manuf. 34 (2020).
[19] Y. Deng, J.-L. Zhang, A. Kaletsch, C. Broeckmann, Modelling and simulation of densification and σ-phase precipitation in PM duplex steel AISI 318LN during hot isostatic pressing, Mater. Today Commun. 29 (102901) (2021).
[20] Quintus, The latest in HIP technology from Quintus, EPMA EuroHIP Seminar, 2020.
[21] A.-H. Puichaud, C. Flament, A. Chniouel, F. Lomello, E. Rouesne, P.-F. Giroux, H. Maskrot, F. Schuster, J.-L. Bechade, Microstructure and mechanical properties relationship of additively manufactured 316L stainless steel by selective laser melting, EPJ Nucl. Sci. Technol. 5 (2019).
[22] T. Cegan, M. Pagac, J. Jurica, K. Skotnicova, J. Hajnys, L. Horsak, K. Soucek, P. Krpec, Effect of hot isostatic pressing on porosity and mechanical properties of 316L stainless steel prepared by the selective laser melting method, Materials 13 (19) (2020).
[23] E. Liverani, A.H.A. Lutey, A. Ascari, A. Fortunato, The effects of hot isostatic pressing (HIP) and solubilization heat treatment on the density, mechanical properties, and microstructure of austenitic stainless steel parts produced by selective laser melting (SLM), Int. J. Adv. Manuf. Technol. 107 (1) (2020) 109–122.
[24] G. Sander, S. Thomas, V. Cruz, M. Jurg, N. Birbilis, X. Gao, M. Brameld, C. R. Hutchinson, On the corrosion and metastable pitting characteristics of 316l stainless steel produced by selective laser melting, J. Electrochem. Soc. 164 (C250) (2017).
[25] M. Laleh, A.E. Hughes, W. Xu, P. Cizek, Y.M. Tan, Unanticipated drastic decline in pitting corrosion resistance of additively manufactured 316L stainless steel after high-temperature post-processing, Corros. Sci. 165 (108412) (2020).
[26] "ASTM B962 - 17 Standard test methods for density of compacted or sintered powder metallurgy (PM) products using Archimedes' principle, ASTM International, 2009.
[27] "ASTM E8 / E8M - 16a Standard Test Methods for tension testing of metallic materials, ASTM International, 2016.
[28] "ASTM E466 - 15 Standard Practice for Conducting Force Controlled Constant Amplitude Axial Fatigue Tests of Metallic Materials, ASTM International, 2021.
[29] B.S.I. Group, Aerospace series. Metallic materials. Test methods. Constant amplitude fatigue testing, BSI Standards Publication,, 2010.
[30] A.J. Bard, L.R. Faulkner. Electrochemical Methods: Fundamentals and Applications, 2nd edition.,, Wiley,, 2001.
[31] ASTM G59 - 97 Standard test method for conducting potentiodynamic polarization resistance measurements, ASTM International, 2020.
[32] ASTM G61 - 86 Test Method for Conducting Cyclic Potentiodynamic Polarization Measurements for Localized Corrosion Susceptibility of Iron-, Nickel-, or Cobalt-Based Alloys, ASTM International, 2018.
[33] C. Elangeswaran, A. Cutolo, G.K. Muralidharan, K. Vanmeensel, B.V. Hooreweder, microstructural analysis and fatigue crack initiation modelling of AM 316L after different heat treatments, Materials and Design, 194, no. ISSN 0264–1275, 2020.
[34] W. Theisen, M. Thiele, C. Esen, R. Hellmann, J. Boes, A. Edelmann, A. Röttger, Microstructure and mechanical properties of 316L austenitic stainless steel processed by different SLM devices, Mater. Sci. Eng. 108 (2020) 769–783.
[35] C. Kanwal, Y. TIan, J.G. Spray, C. Aranas, Effect of annealing heat treatment on the microstructural evolution and mechanical properties of hot isostatic pressed 316L stainless steel fabricated by laser powder bed fusion, Metals 753 (2020) 6.
[36] J. Reijonen, R. Bjorkstrand, T. Riipinen, Z. Que, S. Metsa-Kortelainen, M. Salmi, Cross-testing laser powder bed fusion production machines and powders: variability in mechanical properties of heat-treated 316L stainless steel, Mater. Des. 204 (109684) (2021).
[37] J. Olsén, Additive metallurgy - Thermal influences on structure and properties of stainless steel 316L, Doctoral Thesis in Materials Chemistry at Stockholm University, Sweden, 2020.
[38] L. Cui, S. Jiang, J. Xu, R.L. Peng, R.T. Mousavin, J. Moverare, Revealing relationships betweenmicrostructure and hardening nature of additively manufactured 316L stainless steel, Mater. Des. 198 (109385) (2021).
[39] T. Ronnenber, C.M. Davies, P.A. Hooper, Revealing relationships between porosity, microstructure and mechanical properties of laser powder bed fusion 316L stainless steel through heat treatment, Mater. Des. 189 (108481) (2020).
[40] R.W. Fonda, D.J. Rowenhurst, C.R. Feng, A. Levinson, K. Knipling, S. Olig, A. Ntiros, B. Stiles, R. Rayne, The effects of post-processing in additively manufactured 316L stainless steels, Metall. Mater. Trans. A 51 (2020) 6560–6573.
[41] A. Röttger, K. Geenen, M. Windmann, F. Binner, W. Theisen, Comparison of microstructure and mechanical properties of 316 L austenitic steel processed by selective laser melting with hot-isostatic pressed and cast material, Master Sci. Eng.: A 678 (15) (2016) 365–376.
[42] F. Yang, D. Zhu, M. Jiang, H. Liu, S. Guo, Q. Wang, H. Wang, Zhang Kai, A. Huang, J. Hou, Effect of heat treatment on the microstructure, mechanical properties and corrosion resistance of selective laser melted 304L stainless steel, Acta Metall. Sin. (Engl. Lett.) (2022).
[43] M.J. Higgins, J. Kang, G. Huang, D. Montiel, N. Lu, H. Liu, Y.-F. Shen, P. Staublin, J.-S. Park, J.D. Almer, P. Kenesei, P.G. Sander, R.M. Suter, K. Thornton, A. J. Shanhai, Anomalous strain-energy-driven macroscale translation of grains during nonisothermal annealing, PHYS. Rev. Mater. 5 (2021), L070401.
[44] P.D. Harvey, Engineering Propreties of AISI Type 316L Stainelss Steel, Annealed Sheet, American Society for Metals, Metals Park, Ohio, 1982.
[45] W.D. Callister, Fundamentals of Materials Science and Engineering: An Integrated Approach, Wiley, London, 2000.
[46] Y. Wang, T. Voisin, J.T. McKeown, J. Ye, P.N. Calta, Z. Li, Z. Zeng, Y. Zhang, W. Chen, T.T. Roehling, R.T. Ott, M.K. Santala, P.J. Depond, M.J. Matthews, A. V. Hamza, T. Zhu, Additively manufactured hierarchical stainless, Nat. Mater. 17 (1) (2018).
[47] J.S. Zuback, T. DebRoy, The hardness of additively manufactured alloys, materials 11 (11) (2018).
[48] O. Muransky, L. Balogh, M. Tran, J.-S. Park, M.R. Daymond, On the measurement of dislocations and dislocation substructures using EBSD and HRSD techniques, Acta Mater. 175 (15) (2019) 297–313.
[49] S. Bahl, S. Mishra, K.U. Yazar, I.R. Kola, K. Chatterjee, S. Suwas, Non-equilibrium microstructure, crystallographic texture and morphological texture synergistically result in unusual mechanical properties of 3D printed 316L stainless steel, Addit. Manuf. 28 (2019) 65–77.
[50] K.-T. Kim, Mechanical performance of additively manufactured austenitic 316L stainless steel, Nucl. Eng. Technol. 54 (1) (2022) 244–254.
[51] F.R.N. Nabarro, Dislocations in a simple cubic lattice, Proc. Phys. Soc. 2 (256) (1947) 59.
[52] F.R.N. Nabarro, Fifty-year study of the Peierls-Nabarro stress, Mater. Sci. Eng.: A 234–236 (1997) 67–76.
[53] A.J. Foreman, M.A. Jaswom, J.K. Wood, Factors controlling dislocation widths, Proc. Phys. Sci. Soc. Sect. A 64 (2) (1951) 156–163.
[54] Y. Wang, Y.-t Wang, R.-d Li, P.-d Niu, M.-b Wang, T.-c Yuan, K. Li, Hall-Petch relationship in selective laser melting additively manufactured metals: using grain or cell size? J. Cent. South Univ. 28 (4) (2021) 1043–1057.
[55] M.S. Pham, B. Dovgyy, P.A. Hooper, Twinning induced plasticity in austenitic stainless steel 316L made by additive manufacturing, Mater. Sci. Eng.: A 704 (2017) 102–111.
[56] J. Mishra, V. Balasubramaniyan, Evaluation of Implicit Reliability Level Associated with Fatigue Design Criteria of Nuclear Class-1 Piping, 2018.
[57] Argonne National Laboratory, Effect of LWR Coolant Environments on the Fatigue life of Reactor Materials Final Report, U.S. Nuclear Regulatory Commission Office of Nuclear Regulatory Research Washington, DC 20555–0001, Argonne, Illinois, 2007.
[58] G.S. Frankel, Pitting corrosion of metals: a review of the critical factors, J. Electrochem. Soc. 145 (2186) (1998).
[59] Y.-W. Hao, B. Deng, C. Zhong, Y.-m Jiang, J. Li, Effect of surface mechanical attrition treatment on corrosion behavior of 316 stainless steel, J. Iron Steel Res. Int. 16 (2009) 68–72.
[60] X. Fu, Y. Ji, X. Cheng, C. Dong, Y. Fan, X. Li, Effect of grain size and its uniformity on corrosion resistance of rolled 316L stainless steel by EBSD and TEM, Mater. Today Commun. 25 (101429) (2020).
[61] I.S. Grech, N. Wint, N.P. Lavery, J. Sullivan, S. Mehraban, Evaluating the Corrosion Performance of Wrought and Additively Manufactured (AM) Invar ® and 17–4PH, in Solid Freeform Fabrication Symposium, Austin, Texas, 2019.
[62] G. Sander, J. Tan, P. Balan, O. Gharbi, D.R. Feenstra, L. Singer, R.G. Kelly, J. R. Scully, N. Birbilis, Corrosion of additively manufactured alloys: a review, Corros. J. Sci. Eng. 74 (12) (2018) 1318–1350.
[63] C. Zhao, Y. Bai, Y. Zhang, X. Wang, J.M. Xue, H. Wang, Influence of scanning strategy and building direction on microstructure and corrosion behaviour of selective laser melted 316L stainless steel, Mater. Des. 209 (109999) (2021).
[64] M.G. Fontana, N.D. Greene, Corrosion Engineering, McGraw-Hill, New York, 1967.